

due to repair of the DNA (deoxyribonucleic acid) double-strand breaks, it is typically useful for times only of the order of 24–48 h post exposure (Redon et al. 2009, Schmid et al. 2010), with the effective cut-off time depending on the dose and the method of analysis. The CBMN signal (Figure 1b), by contrast, has a half life of around one year (da Cruz et al. 1994) but the assay currently requires up to three days for processing.

We have therefore designed the RABiT to be able to process either assay, with a rapid switchover between them. Our aim is that all samples collected within the first 24–48 hours post irradiation, will be processed using the γ -H2AX assay (Turner et al. 2011). After the γ -H2AX signal ceases to be useful, the RABiT will be switched over to the CBMN assay (Fenech 2007), and all subsequent samples processed using the CBMN assay (see Figure 1c). To establish the optimal time post exposure to switch between the two assays, we are currently characterising the kinetics of γ -H2AX signal decay in the general population. We are also investigating the possibility of reducing the processing time of the CBMN assay.

The RABiT has been designed for operation as a permanent installation at a central location, with fingerstick blood samples collected in the field and transported to the RABiT (Garty et al. 2011). This allows a more robust installation, removes the need to design the system to withstand transport, and potentially allows use of the RABiT for other applications. Specifically, a long-term goal is that the RABiT may also be used for routine clinical applications in a hospital setting. Such dual usage has major advantages, in terms of both (a) the ability of communities to acquire RABiT systems, and (b) allowing the RABiT system to be in routine use, so that when urgently needed after a radiological event, the machine will be operational and staffed with experienced personnel. Two clinical applications

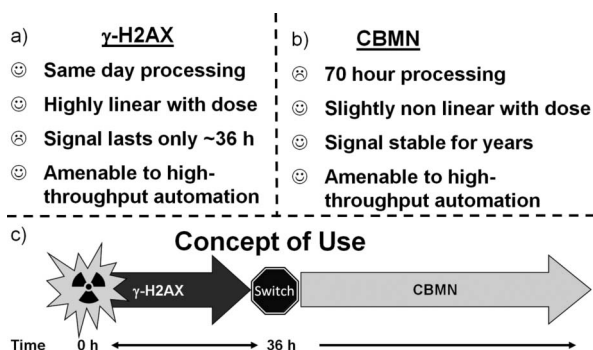


Figure 1. (a) and (b) Characteristics of the Histone H2AX phosphorylation (γ -H2AX) assay and the Cytokinesis Block Micronucleus assay (CBMN) assay. (c) Concept of implementation of the two assays in the RABiT (in this case assuming a 36-hour useful life span of the γ -H2AX assay).

that we foresee are high-throughput multiplexed cytogenetic screening such as for objective, fully-automated, resource-conserving, amniocentesis (Evans et al. 2006), with improved reproducibility over current approaches, and simultaneous profiling of multiple proteins with multiplexed immunoassay screening (Palzer et al. 2005). Initial tests of these endpoints are currently under way. Overall, a dual usage scenario will allow for continuous operation of the RABiT, at low capacity, ensuring appropriate maintenance and the availability of experienced personnel when needed after a radiological event.

This paper describes recent upgrades to the RABiT, resulting in increased throughput and reliability, and outlines the reliability tests that have been performed. Preliminary biodosimetry data collected using the RABiT are described elsewhere (Lyulko et al. 2011, Turner et al. 2011).

System overview

An overview of the RABiT is shown in Figure 2. Capillary-blood samples arrive at the RABiT in a holder, described in the *Materials and methods* section, (Figure 4). After the holders are placed by the RABiT operator in centrifuge buckets on the input stage, no further human intervention is required. A SCARA robot (Selective Compliant Articulated Robot Arm – Stäubli Robotics, Santa Rosa, CA, USA) loads the buckets into a modified centrifuge (Chen et al. 2010b) based on an Eppendorf 5810R (Eppendorf North America, Hauppauge, NY, USA) for lymphocyte enrichment. The buckets, containing capillaries with a separated lymphocyte band, are then transferred by the service robot to a lymphocyte harvest station where each capillary is identified, cut and the lymphocytes dispensed to a

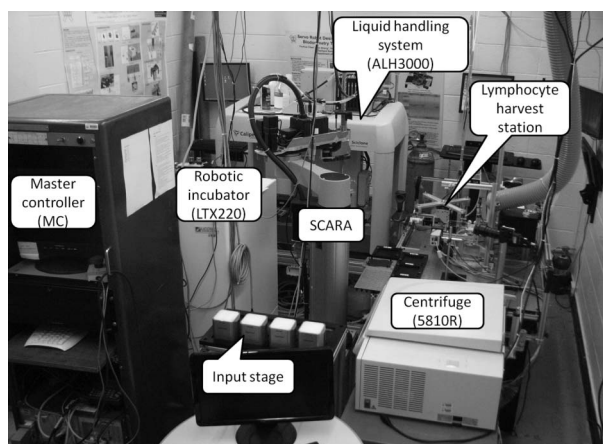


Figure 2. Photo of the RABiT, showing the various subsystems. The Lymphocyte Harvest station is shown in close up in Figure 5. The imaging system is shown in Figure 8. The transfer to substrate system is described in Chen et al. (2010b).

multi-well plate. When all 96 micro-wells are loaded, the multi-well plate is transferred to a Sciclone ALH3000 liquid handling system (Caliper Life Science, Hopkinton, MA, USA) where reagents can be added or removed as needed. An LTX220 robotic incubator (Liconic Instruments, Woburn, MA, USA) is available for lymphocyte culturing in the CBMN assay. After the assay is finished, the multi-well plates, containing fixed, stained lymphocytes, are moved to the transfer-to-substrate system (TTS) (Chen et al. 2010b) where the filter bottoms are removed and sealed between two layers of transparent tape. The lymphocytes are then imaged at $40\times$ using a custom-built imaging system (IS), based on Nikon infinity optics components (shown below in Figure 8, further details provided in the *Materials and methods* section).

The current (2011) version of the RABiT consists of three tiers of hardware (Figure 3) interconnected using six communications protocols. The top tier – central master controller (MC – based on the Real Time Application Interface Linux kernel) – is used to

control, monitor, and record the operation of the system. The middle tier includes all subsystems which have their own controllers, and the actuators directly controlled by the central master controller.

The bottom tier encompasses peripherals under the control of the Second Tier systems (SCARA robot, cell harvesting computer, TTS and IS). Digital cameras use the Camera Link serial communication protocol to transfer pictures to their server computers. Two image storage devices, specifically a 15 Giga Byte Emprise 3000 hard disk array (Xiotech Corporation, Eden Prairie, MN, USA) and T120 tape library (Spectra Logic corporation, Boulder, CO, USA), use extremely high-speed (4 Gigabit per sec) fibre channel links. Large packets of data between the central master computer and subsystem controllers are transferred using the User Datagram Protocol (UDP), while small packets of data are transferred using the Recommended Standard 232 (RS232) protocol.

Three speed bottlenecks were identified in earlier versions of the RABiT:

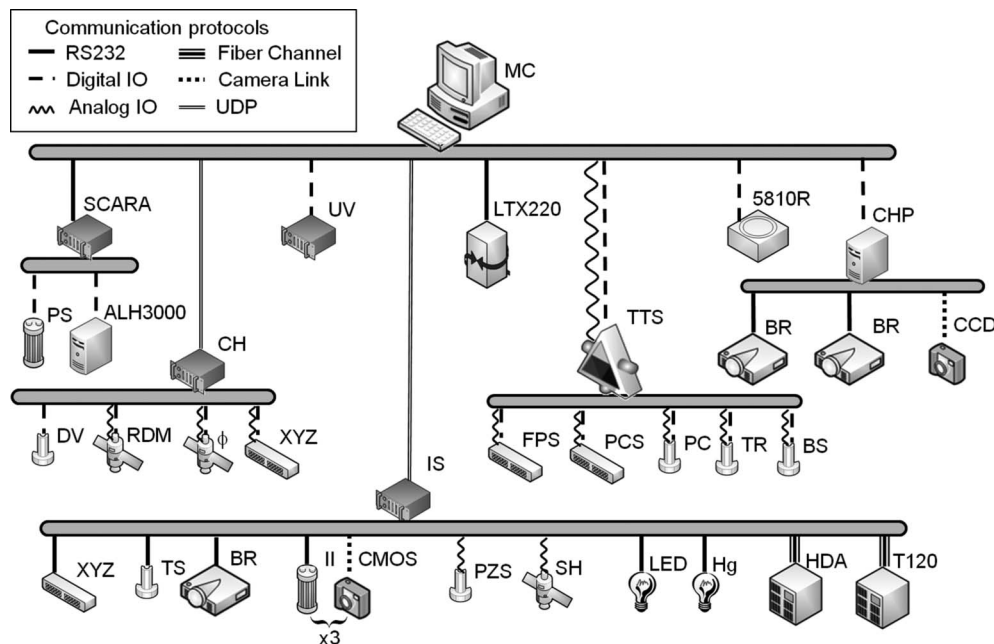


Figure 3. Hardware structure of the RABiT. The top tier (Main Computer, MC) controls the overall operation of the RABiT. Two additional computers control the cell harvesting system (CH, dealing with the robotics and CHP dealing with the capillary imaging and barcode reading). An additional dedicated computer controls the imaging system (IS). The middle tier includes systems with dedicated controllers: The SCARA robot, the Osprey UV laser (UV), The Liconic LTX220 incubator, the Eppendorf 5810R centrifuge and the Caliper Sciclone ALH300. The bottom tier consists of the low-level peripherals: The lymphocyte harvest station is controlled by two computers. The CHP computer controls the two barcode readers (BR) one for reading the plate barcodes and one for reading the capillary barcodes and a CCD camera for imaging the red blood cell band. The CH computer controls a dispensing valve (DV) a rotating drive motor (RDM), an XYZ stage and a rotation stage (Φ). The Transfer to Substrate System (TTS) (Chen et al. 2010b), controlled directly by MC, consists of a feed plate slide (FPS), for loading a plate, a Peel Clamp (PC) and Peel Clamp Slide (PCS) for removing the under drain from the multiwell plate, a Tape Roller (TR) and Barcode Stamp (BS). Finally, the Imaging System (IS) consists of a 3-axis gantry stage (XYZ) and tape spooler (TS) for coarse sample motion, a Piezoelectric Z stage (PZS) for fine focusing and a galvanometric scan head (SH) for fine motions within the sample. A barcode reader (BR) is provided for sample identification. Each image is acquired using an Image intensifier (II) and a CMOS camera (CMOS). Sample illumination is provided from a mercury lamp (Hg) and an ultraviolet light emitting diode (LED). Images are stored on a 15TB hard disk array (HDA) and then transferred to a T120 tape library.

- (1) Sample collection – this is the first stage, performed in the field, where the individuals need to be identified, their blood drawn and packed for shipping to the RABiT.
- (2) Lymphocyte harvesting – this is the second stage of processing in the RABiT, following a centrifugation step. In this stage individual capillaries are extracted from the centrifuge bucket, their barcodes are read, the lymphocyte band is located and the capillary is cut. The bottom of the capillary, containing red blood cells, is discarded, the lymphocytes dispensed to a multi-well plate and the (empty) capillary discarded as well.
- (3) Imaging – in this final stage of sample processing several tens of images from each sample need to be grabbed, analysed and stored.

Common to all of these stages is that handling of individual samples limits throughput. By contrast, during centrifugation, 384 capillaries are centrifuged simultaneously; during liquid handling, transfer to substrate and while transporting samples between the various stages of the RABiT, 96 samples are handled simultaneously. Described below are our solutions and initial benchmarking data for these three bottlenecks.

Materials and methods

Sample collection

In order to facilitate blood collection we have developed a sample collection kit (Figure 4), consisting of lancets, bar-coded, heparin-coated capillary tubes with matched personal data cards and patient-tracking wristbands, alcohol wipes and sample holders for filled capillaries. The kit is designed

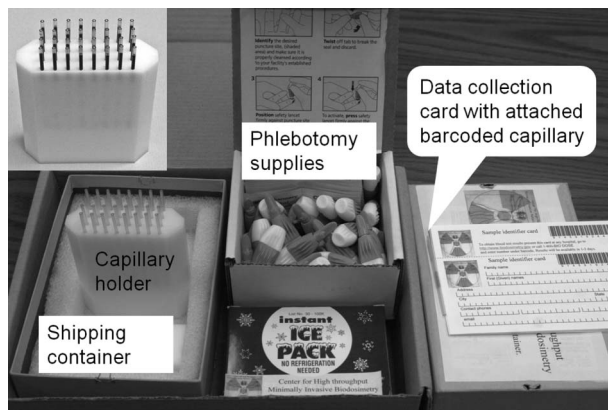


Figure 4. Sample collection kit developed for the RABiT. Shown are the capillary holder (full in insert) with a prototype padded shipping container and ice pack, required phlebotomy supplies and the data collection card with an attached barcoded capillary.

around the 10–15 sample/hour throughput of a single minimally-trained collector, who would use 3–4 such kits in an 8-h shift. See Garty et al. 2011 in this issue for a discussion of how sample collection for the RABiT can be merged into the emergency planning scenarios of a large metropolitan area.

Each individual blood sample is collected into a 100 μ l barcoded Polyvinyl Chloride (PVC) capillary tube (Safe-T-Fill, RAM Scientific, Yonkers, NY, USA). The main advantage of plastic capillary tubes is that they are safer to handle than glass (Jagger and Deitchman 1998). PVC capillaries are also easy to cut and laser-etch, allowing bar-coding and rapid cutting, both of which are required for use in the RABiT.

A capillary holder was designed to serve the dual purpose of facilitating sample collection and shipping as well as an insert for loading multiple capillaries into the RABiT. The holder consists of a plastic block with 32 holes, preloaded with sealing putty (Fisherbrand Hemato-Seal Capillary Tube Sealant, Fisher Scientific, Pittsburgh, PA, USA) and separation medium (Histopaque-1083, Sigma Aldrich, St Louis, MO, USA).

After about 30 μ l of blood is loaded into the capillary, the capillary is inserted into the holder, trapping an air bubble between the blood and separation medium, thus preventing their mixing during shipping. The sealing putty is compressed into and around the capillary ensuring a seal, requiring a weak force (less than 1 Newton) to extract the capillary from the holder. This prevents the capillary from falling out even if the holder is inverted and vigorously shaken, but still allows the RABiT robot to extract the capillary from the holder. This procedure allows the sample to be collected by an individual with minimal training, while maintaining the required layering of the blood and separation medium and preventing contamination. Since only minimally trained personnel are required, many sample collectors may be engaged and work in parallel, increasing sample collection throughput.

Lymphocyte harvesting station

In earlier prototypes of the RABiT (Salerno et al. 2007, Chen et al. 2009, 2010b, Garty et al. 2010), each capillary tube was picked out of the bucket using the SCARA robot, then presented to the barcode reader, then to the imaging camera, and finally to the laser for cutting. The capillary was then located over the appropriate well of the multi-well plate, the lymphocytes dispensed, and the capillary discarded. As this was done sequentially, on individual capillary tubes, this procedure was inefficient and delayed performing other tasks by the SCARA robot, namely, transferring the buckets to

and from the centrifuge and transferring plates to and from the liquid handling system. Using this sequential capillary handling approach, which took ~12 sec per capillary, the maximum throughput was 6,000 samples per 24-h day, where roughly 20 h are spent by the SCARA robot moving capillaries, with the rest of the time spent by the SCARA robot moving buckets and plates.

To overcome this bottleneck, a new scheme for harvesting lymphocytes in fewer than 2 sec/sample was developed, based on the use of a dedicated robot, independent of the SCARA robot. This new scheme also involved an upgrade to the capillary-cutting laser and the development of a new capillary handling station (see Figure 5). This new station processes four capillaries at once and up to 96

capillaries without requiring assistance from the SCARA robot, freeing up the SCARA robot to handle plates and centrifuge buckets exclusively.

The new capillary handling station contains:

- (A) A Cartesian three-dimensional XYZ-stage (Mitsumi, Tokyo, Japan) serving as a movable platform for (i) a centrifuge bucket, containing capillaries, (ii) a micro-well plate, and (iii) a disposing gripper and a trash chute. In this station, lymphocytes are dispensed into a multi-well plate, the empty capillary is discarded and a new capillary is loaded.
- (B) A Charge Coupled Device (CCD) camera (CV-M4+CL, JAI, San Jose, CA, USA) which images the capillary to locate the boundary between red blood cells and separation medium.
- (C) A Hawkeye barcode reader (BR) (Siemens AG, Munich, Germany), which reads the bar code on each capillary.
- (D) A cutting station where an Osprey 2 Watt Ultraviolet (UV) laser (Quantronix Lasers, East Setauket, NY, USA), is used to cut the capillaries, 9 mm above the boundary identified in (B).
- (E) A motorised carousel (Φ -stage, Mitsumi, Tokyo, Japan), with four rotating arms and four capillary grippers, rotates 90° anticlockwise at each step to transfer capillaries to the four work stations (A–D above)

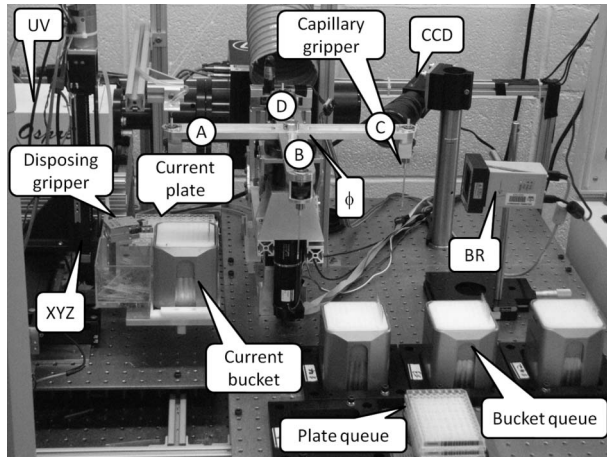


Figure 5. The newly designed lymphocyte harvesting station. Showing the incoming bucket and plate queue, the XYZ stage, with the capillary-filled bucket and plate currently being processed. One capillary is in each of the stations: (A) Lymphocyte dispense, capillary picking and discarding; (B) capillary imaging; (C) barcode reading; and (D) cutting.

Table I presents the timing of the parallel processes performed in the cell harvesting station. In the new scheme, the SCARA robot interacts with the lymphocyte harvest station only by loading empty multi-well plates and removing full ones and by loading full centrifuge buckets and removing the empty ones. This is required once every 96 capillaries (approximately every 3.2 min).

Table I. Timing of new lymphocyte harvest system.

Time [sec]	0	1	2
(A) Cartesian stage (XYZ)	Dispense $i-1$	Dispose of Capillary $i-1$	Index bucket and pick up capillary $i+3$
(B) RBC ¹ detection	Image capillary $i+2$ and detect edge of RBC layer		
(C) Barcode reading	Read barcode on capillary $i+1$		
(D) Laser cutting	Cut capillary i^2		
(E) Pivot head	Rotate 90° Adjust height for $i+1$		

Capillary gripper upgrade

The upgrade to the cell harvesting station also includes a new capillary gripper design, providing better reliability. The capillary gripper is used to manipulate individual capillaries, extracting them from the centrifuge bucket, presenting to the camera, barcode reader and laser cutting system and finally dispensing the lymphocytes into multi-well plates. The details of the design of the original capillary gripper were previously described by Salerno et al. (2007). In the original RABiT system, the capillary gripper was mounted on the end arm of the SCARA robot, whilst in the current design four capillary grippers are mounted on the rotating arms of the Φ stage.

We have modified the capillary gripper from its original design (Figure 6a) by introducing two additional rubber O-rings in the bore of the gripper (Figure 6b). This allows the capillaries to be grabbed with sufficient force to pull them reliably from the bucket inserts. High picking depth (the length of the tube actually in the gripper) leads to a high success rate, but also a higher rate of wear on the O-rings and the plunger (which seals the top of the capillary). The resulting design involved a trade-off between

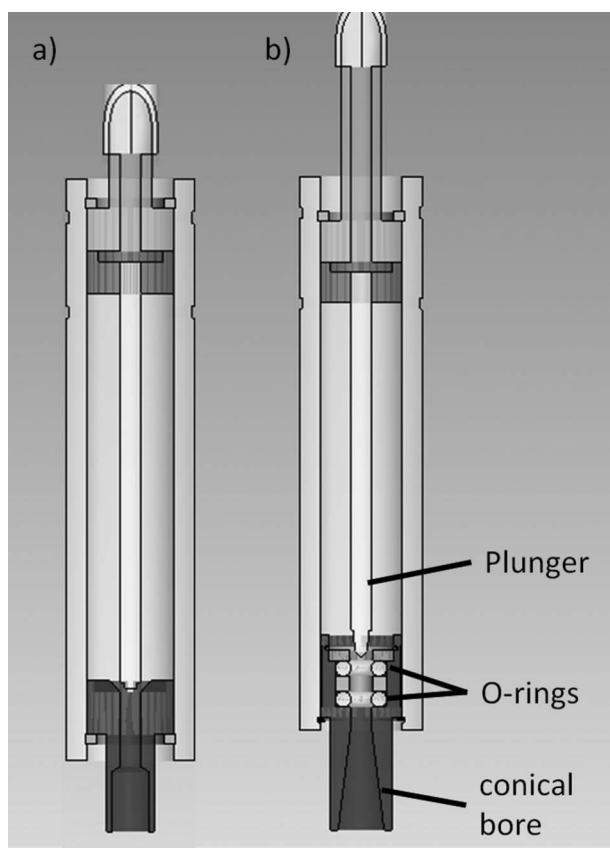


Figure 6. Design drawing of the capillary gripper for (a) the original RABiT (Salerno et al. 2007), and (b) the modified design.

reliability and wear. Additionally, the shape of the bore was changed from cylindrical to conical. This relaxes the required tolerances on gripper alignment with respect to the capillary, as well as the tolerances on the capillary diameter.

In addition to increasing gripper reliability, we have developed an online system for diagnosing capillary picking errors. This system is based on a force/torque sensor, integrated into the gripper, and a Support Vector Machine (SVM) (Burgess 1998) algorithm for error detection. This system is described in more detail in Chen et al. (2010a).

Barcode reading

Prior to cutting the capillaries and dispensing the lymphocytes into one micro-well of a multi-well plate, the barcode on each capillary is read and matched with the barcode and the position of the well on the multi-well plate. Successful reading of this barcode is crucial for automated sample tracking. We have developed a procedure for marking the capillaries using a UV laser similar to the one used for cutting the capillaries, but operated at lower power. A barcode etching spanning roughly 120° of the capillary's circumference is etched using a laser power of 0.7 W. The capillary is then rotated and the process repeated to imprint a barcode on the entire circumference of the tube. Table II shows the various barcodes that we tested for marking the capillaries. Eventually we chose barcode 128C, which is a very high-density barcode symbology, with a smallest element size of 0.2 mm.

Improvement on laser cutting

In addition to the implementation of parallel sample processing, we have increased the speed and reliability of cutting the capillaries. The increase in laser cutting speed was achieved by upgrading the Osprey UV laser (355 nm) used for cutting the capillaries from 1.1–2 W.

Table II. Comparison of barcodes tested.

	Code 128C		Code 25	
Narrow element size	0.2 mm	0.12 mm	0.2 mm	0.12 mm
Width for 10 digit code	20 mm	12 mm	21.4 mm	12 mm
Sensitivity (reads/sec)	2.1	5.75	4.25	2.8
Repeatability	100%	100%	21%	17%
Distance to reader	67 mm	87 mm	66 mm	71 mm
Depth of field	5 mm	3.4 mm	20 mm	11 mm
Reader field of view	1.5 mm	3.6 mm	4.3 mm	9 mm

To increase reliability, the beam is now swept across the diameter of the capillary, as shown in Figure 7, in order to minimise issues resulting from small misalignments of the capillary position and the vibration caused during picking and disposing processes. Once the laser receives the cut command from the central master computer, it sweeps the UV beam with a constant linear speed

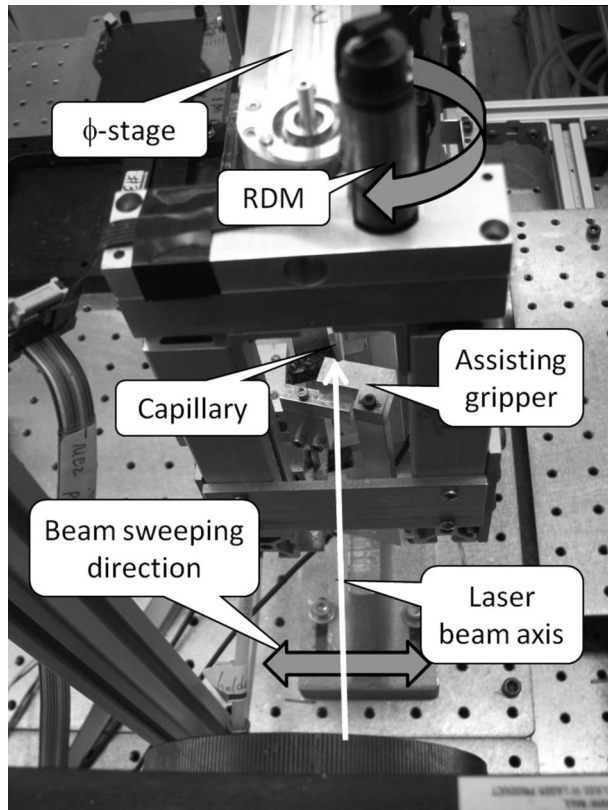


Figure 7. Close-up of the laser cutting station. The Rotating Drive Motor (RDM) is used for spinning the capillary to ensure uniform cutting.

across the capillary tube. At the same time, the capillary gripper rotates with a constant speed in the direction opposite to the direction of the beam sweeping. Optimisation of the two speeds is described in the *Results* section.

We have also introduced an assisting gripper; it clamps on to the bottom part of the capillary at the end of the laser cutting process and facilitates detaching and discarding the bottom part of the capillary, which contains unwanted red blood cells.

Imaging system

High speed imaging is central to the RABiT, and the imaging system has a number of innovative features. Despite much current focus on high-throughput high-content imaging systems (Gough and Johnston 2007, Trask et al. 2009), no commercial system is fast enough with adequate spatial resolution to allow the throughput necessary for the RABiT system. In particular, most current imaging systems acquire images sequentially, using mechanical means to move the sample as well as mechanised cube changers. This results in long lag times (50–500 msec) between image grabs.

We have developed a novel automated imaging system (Figure 8) based on Nikon CFI60 infinity optics components. The use of infinity optics components (Sluder and Nordberg 2007) allows inserting a scan head (SH) and multiple dichroic mirrors and filters in the ‘infinity space’ between the objective (Nikon CFI60 10 \times S-Fluor, Morrell Instruments, Melville, NY, USA) and the tube lens (Edmund optics, Barrington, NJ, USA). An additional Nikon 4 \times relay lens (Morrell Instruments), mounted on each camera, allows achieving a 40 \times magnified image of the lymphocytes. The RABiT imaging system makes use of three new techniques,

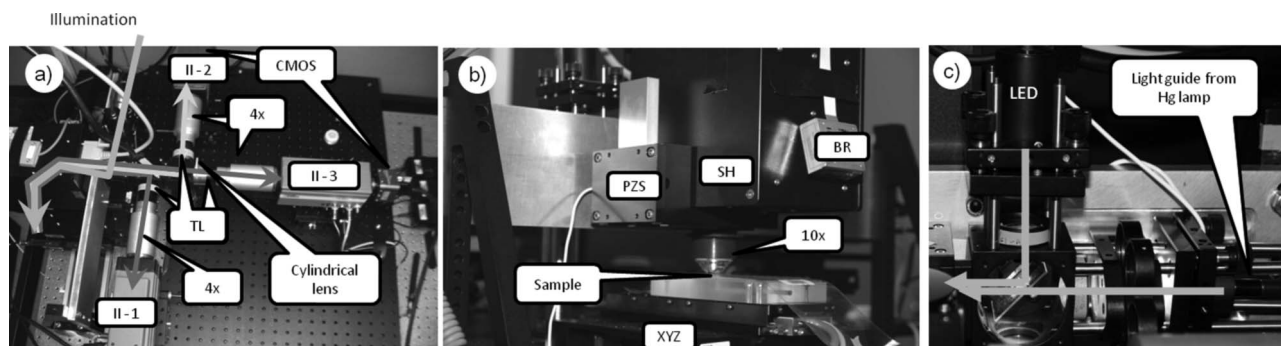


Figure 8. Photos of the RABiT imaging system. (a) Top view showing the illumination light path as well as the three imaging light paths, separated by dichroic mirrors. Each imaging path passes through a 4 \times relay lens and an image intensifier (II) to a CMOS camera. The nucleus is imaged in blue (Hoechst 33342), through a 455 nm emission filter while the cytoplasm or γ -H2AX foci are imaged in orange, through a 585 nm emission filter. The beads used for focusing are imaged through an additional cylindrical lens and 640 nm emission filter. (b) Front view, showing the sample, XYZ stage, Barcode reader (BR), Piezo Z stage (PZS) scan head (SH) and objective (10 \times). (c) Close-up view of the illumination path with the dichroic used for merging light from the UV light emitting diode (LED) exposed.

briefly described here, all of which are critical for speeding up the automated imaging in the RABiT:

- (1) *Light steering.* Within one micro-well, the RABiT images adjacent $200 \times 200 \mu\text{m}$ frames by steering light from off-optical-axis frames into the cameras using fast galvanometric mirrors (SH) (HurryScan II, ScanLab AG, Munich, Germany). This results in typical transit times between adjacent frames of less than 1 msec – two orders of magnitude faster than would be possible with a purely mechanical stage. The light steering technique is facilitated by the splitting of the magnification ($10 \times$ in the objective and an additional $4 \times$ in the relay lens) as the $10 \times$ objective is optimised for aberration-free imaging of a larger area of the sample than would be possible with a $40 \times$ objective. As an example, Figure 9 shows a 4 mm^2 area containing Hoechst-stained cells, plated on the filter bottom of a multi-well plate and imaged using light steering. The scan head is limited to deflections of 1 mm, as described in the *Discussion*. To achieve larger motions (e.g., moving between adjacent samples) a mechanical stage consisting of an LXR404 slide (X axis – 150 mm travel), an MX80 slide (Y axis – 150 mm travel) and a ZP200 Vertical wedge (Z axis – 25 mm travel) (Parker-Hannifin Corp, Rohnert Park, CA, USA) is used.
- (2) *Multiple cameras in parallel.* The RABiT imaging system uses multiple fast Complementary Metal-Oxide Semiconductor (CMOS) cameras

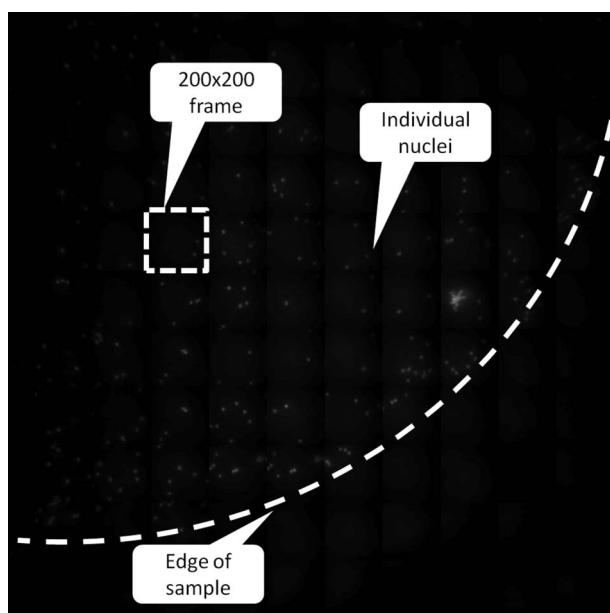


Figure 9. Image of a $2 \times 2 \text{ mm}$ region of a filter containing stained lymphocytes, stitched from 100 individual images. The edge of the 9 mm diameter filter is marked by a dashed line.

(MV D1024-160 CL, Photonfocus AG, Lachen, Switzerland), coupled to image intensifiers (II – VS-1485, Videoscope International, Dulles, VA, USA) capturing images, produced by different fluorophores and separated using Brightline dichroic mirrors and filters (Semrock, Inc, Rochester, NY, USA). For the γ -H2AX assay, this allows simultaneous imaging of the nuclei using Hoechst 33342 (Invitrogen, Carlsbad, CA, USA) and γ -H2AX foci using Alexa Fluor 555 (Invitrogen), while for the CBMN assay, the nuclear stain Hoechst 33342 and the cytoplasmic stain CellMask Orange (Invitrogen) are used. Given that the staining protocols for both bioassays are optimised to use equivalent illumination and filters, this allows the RABiT to be rapidly switched from the γ -H2AX to the CBMN assay in less than 1 h, by just loading new reagents and using alternate software routines. To facilitate high speed imaging, the RABiT uses an intense UV light source based on a high intensity Light Emitting Diode (LED) (Hamamatsu Photonics, Bridgewater, NJ, USA) to excite the nuclear stain (5 mW on the sample); this allows a faster image grab in the nuclear channel. For cytoplasm/ γ -H2AX imaging the green line from an Excite 120PC mercury lamp (Exfo life Science, Toronto, ON, Canada) is used, which provides 60 mW on the sample. The beams from the two light sources are joined using a dichroic mirror (Semrock, Inc), as shown in Figure 8c. Since each sample is illuminated for only a few seconds, photobleaching is not a concern.

- (3) *Single-step autofocus.* Automated focusing is usually a relatively slow iterative process, involving moving the objective towards and away from the stage until best focus is obtained. A faster approach that we have developed is to use a cylindrical lens – a circular bead imaged in focus through a cylindrical lens will appear circular, but when out of focus, it will appear as an ellipse whose aspect ratio defines the distance to the focal plane. Based on the measured aspect ratio, the objective lens is moved using an OP100 piezoelectric Z stage (PZS – Mad City Labs, Madison, WI, USA).
- (4) *Image analysis.* To accelerate image processing and to minimise dead time due to the control and monitoring software, the imaging system software is run on a dedicated high speed Dual Quad core computer (Micro Disc Inc, Yardley, PA, USA), running Linux (Red Hat, Raleigh, NC, USA). Most of the image processing steps, for the nuclear and γ -H2AX/cytoplasm images, are performed on a Matrox Helios xCL (Matrox Imaging Systems Ltd, Dorval, QC, Canada)

frame grabber with on-board pixel processing. A Solios xCL framegrabber (Matrox Imaging Systems Ltd) with an on-board Field-Programmable Gate Array (FPGA) is used for asynchronous processing of the focus information.

Image analysis software

The image analysis software for the RABiT was written in the C programming language and utilises the image processing and image analysis capabilities of the Matrox Imaging Library (MIL 9.0; Matrox Imaging Systems Ltd) with part of the analysis performed in the frame grabber itself. As noted above, image analysis is performed based on a two-colour image, with one colour corresponding to the nuclear image and the second corresponding to either the cytoplasmic image (for CBMN analysis) or γ -H2AX fluorescence. When analysing micronuclei, this approach provides more reliable identification of binucleated cells, compared to staining the nuclei alone. When analysing γ -H2AX fluorescence this approach allows scoring cells with no fluorescence (unirradiated cells or cells in which the damage has been repaired) and also allows elimination of spontaneous fluorescence (e.g., dirt on the sample) which is not correlated with a nucleus.

The algorithm used for analysing γ -H2AX fluorescence, described in detail in (Turner et al. 2011) is based on integration of the total fluorescence of AlexaFluor 555 stained antibodies within the boundaries of each nucleus. This is a simpler, faster and more reliable (at high doses) (Rogakou et al. 1998, Andrievski and Wilkins 2009) approach than the more common foci-counting, which requires high-resolution 3D imaging (Böcker and Iliakis 2006, Hou et al. 2009, Roch-Lefèvre et al. 2010) and underestimates doses above about 2 Gy due to focus overlap (MacPhail et al. 2003, Böcker and Iliakis 2006). Calibrated orange fluorescent beads (Spherotech, Inc., Lake Forest, IL, USA) are used to monitor variations in illumination intensity that are related to the 2,000-h lifetime of the mercury lamp and correct the measured fluorescence accordingly.

Our automated algorithm for scoring micronuclei follows the standard criteria for scoring micronuclei in binucleated (once-divided) cells, as described by Fenech et al. (2003) and Fenech (2007). The actual algorithm used is described by Lyulko et al. (2011). Briefly, nuclei are imaged as before, each nucleus is associated with a single cell (imaged in orange) and the sizes of all nuclei within a single cell compared to determine the number of binucleated cells (two equally sized nuclei) and the number of micronuclei.

Results

The focus of this paper is to describe the technical upgrades to the RABiT and recent reliability tests performed on it. Validation of the biodosimetry assays and first dose-response curves measured using the two assays are described in Lyulko et al. (2011) (CBMN) and Turner et al. (2011) (γ -H2AX).

No blood leakage

When processing capillaries in the RABiT, there is a potential for leakage during centrifugation, where the blood in the capillary experiences acceleration of 3000 *g*. We have monitored all capillaries run through the RABiT and in about 5% there was minor penetration of Red Blood Cells into the sealing putty, but no leakage of lymphocyte separation media or lymphocytes out of the capillary.

Additionally, there is a possibility for leakage following the cutting stage, when the bottom of the capillary is open. To prevent leakage at this stage, the capillary gripper contains a plunger (see Figure 6) which seals the top of the capillary. Surface tension forces then prevent leakage from the capillary until the plunger is removed, and pressurised air is inserted into the top of the capillary, when the capillary is above the appropriate well. No leakage was seen using this system.

Reliability of capillary picking

Figure 10 shows the force required to pull a capillary out of the centrifuge bucket in the lymphocyte harvest module. Table III shows the capillary picking success rate for the original (Figure 6a) and modified (Figure 6b) gripper, for various speeds of the handling robot and for various picking depths.

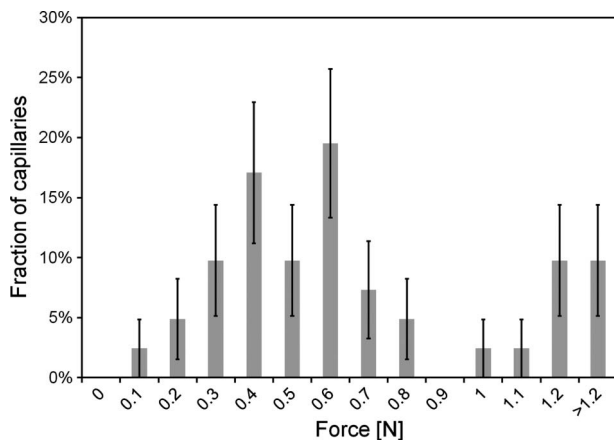


Figure 10. Force required to extract capillaries from the centrifuge bucket. The error bars correspond to the standard error $\pm \sqrt{p \times (1 - p)/N}$, where p is the value of each bar in the histogram and $N=41$ is the number of trials.

Reliability of capillary cutting

For a given laser power (1.9 W) and cutting time (1.7 sec) we have tested various laser sweeping and capillary rotation speeds (see Figure 7). Table IV shows the success rate for cutting 32 capillaries. Based on these measurements, we have selected operational settings of 55 rpm and 0.9 mm/s. Overall, using the higher laser power, the swept beam, and the assisting gripper, we have reduced the cutting time from 3.5 to 1.7 sec while improving the success rate to >99%.

Table III. Success rate of picking capillaries.

Gripper Picking depth	Fig 6a		Fig 6b	
	12 mm		15 mm	
Time to pick	0.03 sec	0.02 sec	0.3 sec	0.15 sec
Old design	61 ± 8% ¹	52 ± 9%	not tested	not tested
New design	99 ± 2%	97 ± 3%	95 ± 4%	93 ± 4%

¹The error estimates correspond to the 95% confidence interval: $\pm 1.96 \times \sqrt{p \times (1-p)/N}$, where p is the measured rate of success and $N=128$ is the number of trials.

Table IV. Success rate of laser cutting.

Rotation speed	Sweeping speed					
	0.5 mm/s	0.75 mm/s	0.8 mm/s	0.9 mm/s	1 mm/s	1.5 mm/s
40 rpm	100 [†] %	100%	60%	80%	100%	60%
45 rpm		80%	80%	80%	100%	
50 rpm		60%	80%	80%	100%	
55 rpm		80%	100%	100%	100%	
60 rpm	60%	100%	60%	80%	100%	100%
80 rpm	100%	100%			100%	60%

[†]95% confidence interval: ±17%, ±13% and + 0%/−10% for 60%, 80% and 100%, respectively. Based on 32 capillaries for each condition.

Sample imaging – focus system

The focusing system uses fluorescent spherical beads interspersed with the lymphocytes. In order to calibrate the autofocus system, we used 10 μm crimson fluorescent beads (Invitrogen). Images were taken at 1/2 μm intervals over a range of 100 μm around the focal plane. For example, Figure 11 shows single 10 μm beads imaged through a 1000 mm cylindrical lens (Thorlabs, Newton, NJ, USA) at 20 μm above focus (Figure 11a), at focus (Figure 11b), and at 20 μm below focus (Figure 11c). Figure 12 shows the measured aspect of a bead as the objective lens is moved across focus as well as the apparent size of a lymphocyte nucleus co-planar with the bead and imaged simultaneously.

Sample motion during imaging

Figure 13 shows the measured time to perform a given deflection. A deflection of 200 μm (360 μsec) corresponds to motion from one field of view to the adjacent one. A deflection of 1 mm (~800 μsec) corresponds to ‘resetting’ the scan head after 100 images were taken.

The mechanical stage used to augment the scan head for deflections above ±1 mm requires 50 msec to perform a 9 mm motion (the distance between two adjacent wells in a multi-well plate).

Changing of the lens position is done via a fast piezo-actuator. Figure 14 shows the time required for a 100 μm vertical motion of the objective lens. 12.6 msec are required to reach 90% of the required motion. This settling time does not depend on the magnitude of the motion. We have seen that typical deflections required for maintaining focus when imaging a filter bottom of a multi-well plate are 12 μm.

A full benchmarking of the RABiT imaging system, including image acquisition and image analysis is currently under way.

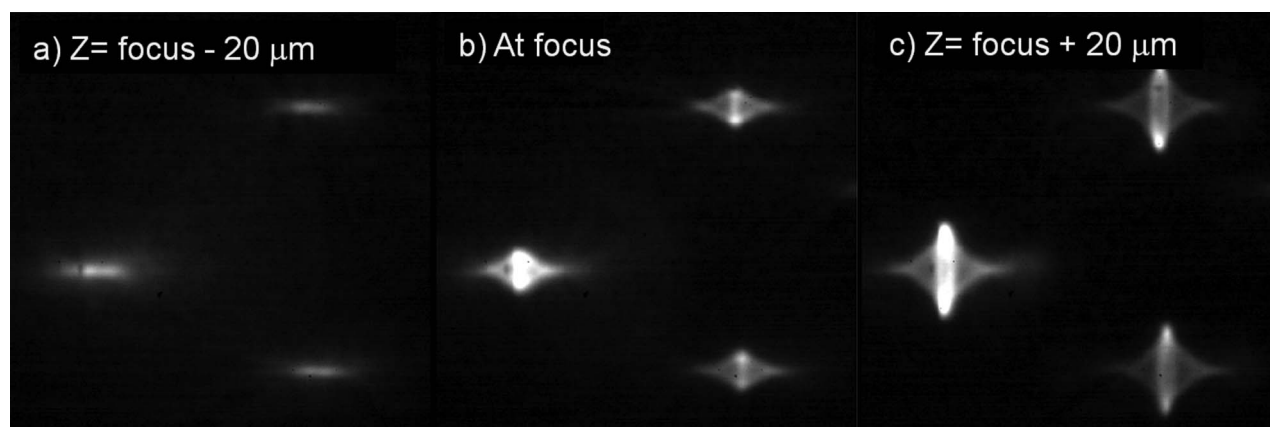


Figure 11. Images of 10 μm beads through a cylindrical lens. The Z-values correspond to the position of the objective lens, mounted on a piezo-actuator.

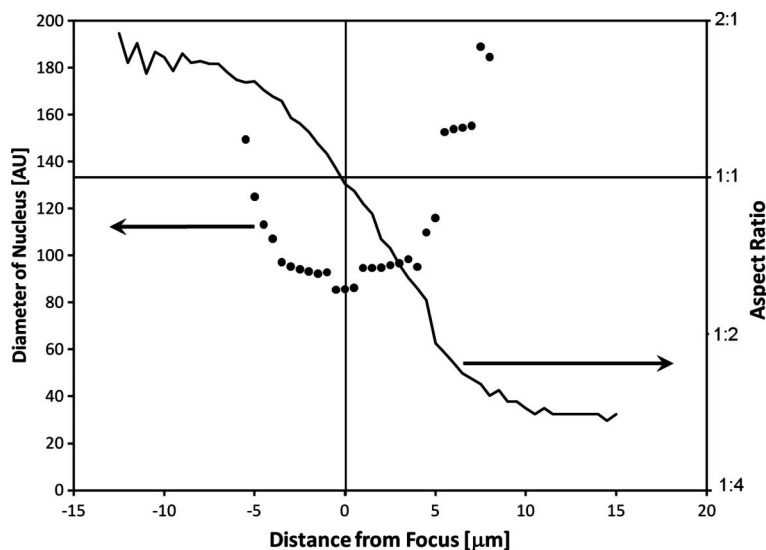


Figure 12. Measured aspect ratio of 10 μm fluorescent beads as a function of objective lens position (line). The values shown correspond to the vertical extent of a bead image divided by its horizontal extent. As a comparison, the symbols show the apparent diameter of a lymphocyte nucleus, imaged simultaneously, on a second camera. Beyond $\pm 5 \mu\text{m}$ or so, the image of the nucleus becomes too fuzzy to extract a diameter.

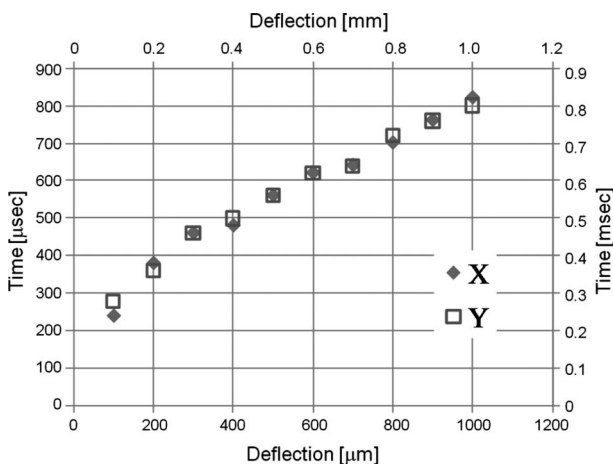


Figure 13. Settling time of the scan head as a function of deflection distance along the two axes.

Sample imaging

Recently, we have used the RABiT system to measure γ -H2AX fluorescence labeling in lymphocyte nuclei from blood samples collected from four healthy female donors, irradiated *ex vivo* with a range of γ -ray doses between 0 and 8 Gy (Turner et al. 2011). Figure 15 shows sample images of lymphocytes, irradiated to 0, 2 and 5 Gy and processed using the RABiT γ -H2AX assay (see Turner et al. 2011 for exact protocol), in filter bottom multi-well plates and then imaged using the RABiT imaging system. The Figure shows representative γ -H2AX fluorescent images captured, in the RABiT, as 12-bit monochrome images (using green illumination and viewing through a 585 nm

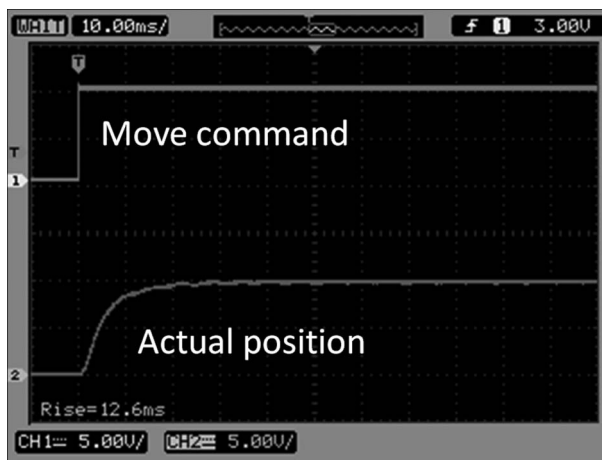


Figure 14. Settling time for the piezoelectric Z stage (PZS) following a 100 μm motion of the objective lens. The upper curve corresponds to the requested position whilst the lower curve corresponds to the actual position. One vertical division corresponds to 50 μm . One horizontal division corresponds to 10 msec.

filter). The images also show an overlaid outline of the nuclear image (as generated by the RABiT image analysis routines).

Discussion

The Rapid Automated Biodosimetry Tool (RABiT) is a fully automated, ultra-high throughput robotically-based biodosimetry workstation. It screens fingerstick-derived blood samples, either to estimate past radiation dose, or to sort individuals exposed above or below a cut-off dose. The RABiT automates two mature, but currently manual,

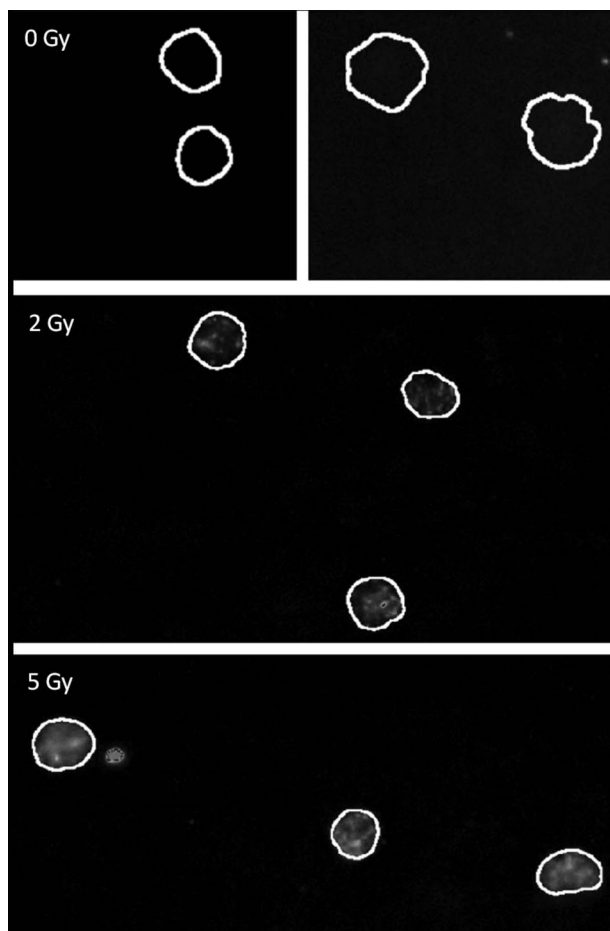


Figure 15. Images of irradiated lymphocytes (0, 2 and 5 Gy), processed using the RABiT γ -H2AX assay protocol, as described in Turner et al. (2011), and imaged using the RABiT imaging system. The outlines around each nucleus were generated from the nuclear image (not shown) by the RABiT software. Fluorescence is integrated within these boundaries. The right hand half of the 0 Gy panel shows an image with the gain increased in post processing to show that the non-irradiated lymphocytes do not have any fluorescence above background. The other panels have not had any post processing other than background subtraction performed in the RABiT and reduction from 12 to 8 bits.

biodosimetry assays (CBMN and γ -H2AX), both of which have been shown to be highly radiation-specific. In designing the RABiT we have taken a comprehensive approach. In addition to the robotic sample handling and analysis, we have developed and tested a sample collection kit, as well as transport procedures that are compatible with high throughput collection in a disaster environment, while maintaining sample integrity. In order to upgrade the RABiT's throughput from a few thousand samples per day, we have located three bottlenecks in the RABiT sample flow, namely, sample collection, lymphocyte isolation and imaging.

This paper describes our approach for accelerating these three processes. We also describe the reliability tests performed on the capillary handling

and tracking. Biological tests of the automated lymphocyte processing in multi-well plates are given elsewhere (Lyulko et al. 2011, Turner et al. 2011).

Sample integrity

A major concern in RABiT design was to avoid blood leakage from the capillaries both during shipping and during processing in the RABiT. This is important to prevent cross contamination and loss of samples, as well as being a safety issue for the RABiT operator and maintenance personnel. In theory, because the bottom of the capillary is sealed, the blood and separation medium cannot leak out of the top during shipping due to surface tension. Our tests have confirmed this both in the lab and in the field.

To demonstrate this, we have tested leakage during blood shipping (Garty et al. 2010), by collecting 32 (unirradiated) blood samples and shipping them, using a commercial carrier from Arizona to New York. None of the samples leaked during shipping and all samples maintained the required layering of blood and separation medium, allowing efficient separation of lymphocytes from red blood cells. The lymphocytes were then cultured to division and formed binucleated cells.

Another aspect of sample integrity is that of the viability of lymphocytes during shipping, in particular for the CBMN assay where the lymphocytes must be healthy enough to divide. Additionally, the yield of phosphorylated H2AX was seen in many studies to decrease with time (Redon et al. 2009, 2010) due to repair of the DNA double-strand breaks. While this cannot be prevented prior to the blood draw, it can be greatly reduced by storing the blood at low temperatures (Moroni et al. 2008). We therefore envisage shipping the blood samples chilled, in containers similar to those used for shipping vaccines (Kendal et al. 1997). A comprehensive study, comparing different shipping modalities is currently under way. The logistics of sample collection and shipping are discussed elsewhere in this issue (Garty et al. 2011).

A second major concern is sample tracking. Each capillary is marked with a barcode, corresponding to a specific individual's contact info. The reliable reading of this barcode, prior to cutting the capillary, is therefore of utmost importance. In the RABiT, we have achieved a success rate of >95% for reading the bar codes (Chen et al. 2009). The misread barcodes are due to improper angular orientation of the capillary – the barcode reader is facing the seam between two barcode etchings. This inaccuracy will be resolved by rotating the capillary

during the barcode reading. The filter-bottomed multi-well plates and the sealed imaging substrates are also marked with a barcode and barcode readers are installed at the entrances to all RABiT subsystems.

Lymphocyte harvesting

In a previous work (Garty et al. 2010), we have reported on an efficient separation of the lymphocytes within the capillary. In order to transfer these lymphocytes to a multi-well plate, we must first successfully extract the capillary from the centrifuge bucket, then cut the capillary and finally dispense the lymphocytes into the well.

The large variation seen in the force required for extracting the capillary from its holder (Figure 10) stems from variations in both capillary diameter ($\pm 30 \mu\text{m}$, due to the extrusion process) and the amount of putty used to seal the capillary bottom (loaded manually). The force required to extract the capillary is directly related to the area of the capillary over which the putty is bound. Nevertheless, in no case did we see that the binding was too strong for the gripper arm to successfully extract the capillary.

The lymphocyte harvesting station has been changed significantly from the one described previously (Chen et al. 2009, 2010b, Garty et al. 2010). It now consists of a standalone robot whose sole purpose is to handle the capillaries. This enabled processing of four capillaries in parallel as well as freeing up the SCARA robot to perform other tasks.

Although the new robot is slower than the SCARA robot at picking capillaries, the reliability of capillary picking has been significantly improved, with 1–5% of capillaries not picked on the first attempt (compared to almost a half with the old design). This is typically due to small misalignments between the capillary and the gripper. An online rapid failure detection system (Chen et al. 2010a) was designed to trap this error and perform a second attempt at picking the capillary in case of failure. Since the capillary picking time is still shorter than the cutting time, this has no impact on throughput.

An improvement in both cutting speed and reliability has also been shown in this work.

As described in detail in Turner et al. (2011), the lymphocytes released from the capillary into the multi-well plate showed: (i) Sufficient lymphocyte number to perform the assay, (ii) adequate dispersal, and (iii) good cellular morphology. In particular, we have seen no difference in lymphocyte morphology when comparing lymphocytes from capillaries cut with a blade to those from capillaries cut using the laser. This confirms our previous calculations that the laser does not significantly heat the lymphocytes.

Imaging

A key component of the RABiT's imaging system is the simultaneous acquisition of images using different stains and multiple cameras. As both image analysis algorithms (γ -H2AX and CBMN) require the two stain images to be matched, proper alignment of the two cameras is vital. We routinely use multispeck fluorescent beads (Invitrogen), to measure alignment of the RABiT cameras. At the beginning of each session of imaging, we grab images of the beads and verify alignment. Using this method, alignment of the two images with a precision of 5 pixels (roughly $1 \mu\text{m}$) is typically achieved.

Focusing

A major rate-limiting step in high-throughput imaging systems is the focusing process. In order to get good image quality, typical microscope objective lenses have a shallow depth of field and may therefore be sensitive to the roughness of the sample being imaged. This is noticeable when imaging cells on a microscope slide which may be slightly tilted and becomes a serious problem for imaging rough substrates, such as the filter bottoms of multi-well plates. The typical solution in automated imaging systems is to grab a series of images at different focal planes and select the best one. This is obviously not compatible with high throughput.

Our solution, of interspersing fluorescent beads within the sample and imaging them through a cylindrical lens, allows making rapid on-line focus corrections. The aspect ratio of the beads is continuously monitored. If a bead appear as a vertical (horizontal) ellipse, the objective can be moved up (down) rapidly before the next image is taken. Furthermore, the value of the aspect ratio (see Figure 12) can be used to determine the extent of the motion. The range of accuracy of this method is, in our case, about $\pm 30 \mu\text{m}$, which is larger than the $\sim 10 \mu\text{m}$ variations we have seen when imaging actual filters. It should be noted that the emission spectrum of the crimson fluorescent beads (Invitrogen) used for monitoring the focus quality is sufficiently separated from the emission spectrum of the nuclear, cytoplasmic and AF555 stains used and therefore bead images do not appear in the other cameras.

Sample motion during imaging

As noted above, mechanical motion in an automated microscope system typically takes tens of msec. We have overcome this by performing 99% of sample motion using a galvanometric scan head (namely imaging a 10×10 array of frames, using the scan head, for every motion using the mechanical stage).

We have limited the deflection to ± 1 mm or less on both axes. At larger deflections, due to the short working distance of the objective used (1.2 mm; Nikon S Fluor 10 \times ; Morell Instruments), the light is collected into the objective lens at an angle approaching 45°, resulting in coma aberrations. This limit was seen both in simulations and in the actual RABiT imaging system.

Conclusions

Over the past five years the Columbia Center for Minimally Invasive Radiation Biodosimetry has developed the RABiT, a completely automated, ultra-high-throughput biodosimetry workstation. The RABiT analyses fingerstick-derived blood samples to estimate past radiation exposure or to identify individuals exposed above or below a cut-off dose.

Here we have described ongoing upgrades made to the RABiT, with the goal of increasing its throughput from 6,000 to 30,000 samples per day, while maintaining or improving reliability. Specifically, we have streamlined and, wherever possible, parallelised all stages of the RABiT where individual samples are handled (sample collection, lymphocyte harvest and the imaging system). The current RABiT (2011) is undergoing extensive benchmarking and reliability tests, and a large scale demographic study is in preparation for establishing RABiT calibration curves for both assays.

Acknowledgements

This work was supported by grant number U19 AI067773 to the Center for High-Throughput Minimally Invasive Radiation Biodosimetry from the National Institute of Allergy and Infectious Diseases/National Institutes of Health.

Declaration of interest: The authors report no conflicts of interest. The authors alone are responsible for the content and writing of the paper.

References

Andrievski A, Wilkins RC. 2009. The response of γ -H2AX in human lymphocytes and lymphocytes subsets measured in whole blood cultures. *International Journal of Radiation Biology* 85:369–376.

Böcker W, Iliakis G. 2006. Computational methods for analysis of foci: Validation for radiation-induced γ -H2AX foci in human cells. *Radiation Research* 165:113–124.

Burges CJC. 1998. A tutorial on support vector machines for pattern recognition. *Data Mining and Knowledge Discovery* 2:121–167.

Chen Y, Wang H, Zhang J, Pile JA, Garty G, Simaan N, Yao YL, Brenner DJ. 2010a. Automated recognition of robotic manipulation: Failure modes in high-throughput biodosimetry tool. *Engineering Applications of Artificial Intelligence* (Submitted).

Chen Y, Zhang J, Wang H, Garty G, Xu Y, Lyulko OV, Turner HC, Randers-Pehrson G, Simaan N, Yao YL, Brenner DJ. 2009. Design and preliminary validation of a rapid automated biodosimetry tool for high throughput radiological triage. *Proceedings of the American Society of Mechanical Engineers* 3:61–67.

Chen Y, Zhang J, Wang H, Garty G, Xu Y, Lyulko OV, Turner HC, Randers-Pehrson G, Simaan N, Yao YL, Brenner DJ. 2010b. Development of a robotically-based automated biodosimetry tool for high-throughput radiological triage. *International Journal of Biomechanics and Biomedical Robotics* 1:115–125.

da Cruz AD, McArthur AG, Silva CC, Curado MP, Glickman BW. 1994. Human micronucleus counts are correlated with age, smoking, and cesium-137 dose in the Goiania (Brazil) radiological accident. *Mutation Research/Environmental Mutagenesis and Related Subjects* 313:57–68.

Evans MI, Sharp M, Tepperberg J, Kilpatrick MW, Tsiouras P, Tafas T. 2006. Automated microscopy of amniotic fluid cells: Detection of FISH signals using the FastFISH imaging system. *Fetal Diagnosis and Therapy* 21:523–527.

Fenech M. 2007. Cytokinesis-block micronucleus cytome assay. *Nature Protocols* 2:1084–1104.

Fenech M, Chang WP, Kirsch-Volders M, Holland N, Bonassi S, Zeiger E. 2003. HUMN project: Detailed description of the scoring criteria for the cytokinesis-block micronucleus assay using isolated human lymphocyte cultures. *Mutation Research* 534:65–75.

Garty G, Chen Y, Salerno A, Turner H, Zhang J, Lyulko OV, Xu Y, Wang H, Simaan N, Randers-Pehrson G, Yao YL, Amundson SA, Brenner DJ. 2010. The RABiT: A rapid automated biodosimetry tool for radiological triage. *Health Physics* 98:209–217.

Gough AH, Johnston PA. 2007. Requirements, features, and performance of high content screening platforms. *Methods in Molecular Biology* 356:41–61.

Grace MB, Moyer BR, Prasher J, Cliffer KD, Ramakrishnan N, Kaminski J, Coleman CN, Manning RG, Maidment BW, Hatchett R. 2010. Rapid radiation dose assessment for radiological public health emergencies: Role of NIAID and BARDA. *Health Physics* 98:172–178.

Hou Y-N, Lavaf A, Huang D, Peters S, Huq R, Friedrich V, Rosenstein BS, Kao J. 2009. Development of an automated γ -H2AX immunocytochemistry assay. *Radiation Research* 171:360–367.

Jagger J, Deitchman S. 1998. Hazards of glass capillary tubes to health care workers. *Journal of the American Medical Association* 280:31–31.

Garty G, Karam PA, Brenner DJ. 2011. Infrastructure to support ultra high throughput biodosimetry screening after a radiological event. *International Journal of Radiation Biology* submitted.

Kendal AP, Snyder R, Garrison PJ. 1997. Validation of cold chain procedures suitable for distribution of vaccines by public health programs in the USA. *Vaccine* 15:1459–1465.

Lyulko OV, Garty G, Randers-Pehrson G, Turner H, Brenner DJ. 2011. Fast image analysis for the micronucleus assay in a fully automated high-throughput biodosimetry system. *Radiation Research* (Submitted).

MacPhail S, Banath J, Yu T, Chu E, Lambur H, Olive P. 2003. Expression of phosphorylated histone H2AX in cultured cell lines following exposure to x-rays. *International Journal of Radiation Biology* 79:351–358.

Moroni MM, Krasnopolsky K, Subramanian U, Martin PR, Doherty KM, Prasanna PGS. 2008. Does cell culture type and blood transport temperature affect dicentric yield and radiation dose assessment? *Journal of Medical, Chemical, Biological and Radiological Defense* 6. Accessed 14 February 2011 from the website: <http://www.jmedcbr.org>.

Palzer S, Bailey T, Hartnett C, Grant A, Tsang M, Kalyuzhny AE. 2005. Simultaneous detection of multiple cytokines in elispot assays. *Methods in Molecular Biology* 302:273–288.

- Rea ME, Gougelet RM, Nicolalde RJ, Geiling JA, Swartz HM. 2010. Proposed triage categories for large-scale radiation incidents using high-accuracy biodosimetry methods. *Health Physics* 98:136–144.
- Redon CE, Dickey JS, Bonner WM, Sedelnikova OA. 2009. γ -H2AX as a biomarker of DNA damage induced by ionizing radiation in human peripheral blood lymphocytes and artificial skin. *Advances in Space Research* 43:1171–1178.
- Redon CE, Nakamura AJ, Gouliava K, Rahman A, Blakely WF, Bonner WM. 2010. The use of gamma-H2AX as a biodosimeter for total-body radiation exposure in non-human primates. *PLoS ONE* 5:e15544.
- Roch-Lefèvre S, Mandina T, Voisin P, Gaëtan G, Mesa JEG, Valente M, Bonnesoeur P, García O, Voisin P, Roy L. 2010. Quantification of γ -H2AX foci in human lymphocytes: A method for biological dosimetry after ionizing radiation exposure. *Radiation Research* 174:185–194.
- Rogakou EP, Pilch DR, Orr AH, Ivanova VS, Bonner WM. 1998. DNA double-stranded breaks induce histone H2AX phosphorylation on serine 139. *Journal of Biological Chemistry* 273:5858–5868.
- Salerno A, Zhang J, Bhatla A, Lyulko OV, Dutta A, Garty G, Simaan N, Pehrson GR, Yao YL, Brenner DJ, Nie J. 2007. Design considerations for a minimally invasive high-throughput automation system for radiation biodosimetry. *IEEE International Conference on Automation Science and Engineering, CASE 2007*. pp 846–852.
- Schmid TE, Dollinger G, Beisker W, Hable V, Greubel C, Auer S, Mittag A, Tarnok A, Friedl AA, Molls M, Roper B. 2010. Differences in the kinetics of gamma-H2AX fluorescence decay after exposure to low and high let radiation. *International Journal of Radiation Biology* 86:682–691.
- Sluder G, Nordberg JJ. 2007. *Microscope basics*. In: Greenfield S, David EW, editors. *Methods in cell biology*. New York: Academic Press. pp 1–10.
- Trask OJ, Nickischer D, Burton A, Williams RG, Kandasamy RA, Johnston PA. 2009. High-throughput automated confocal microscopy imaging screen of a kinase-focused library to identify p38 mitogen-activated protein kinase inhibitors using the GE incell 3000 analyzer. *Methods in Molecular Biology* 565:159–186.
- Turner HC, Brenner DJ, Chen Y, Bertucci A, Zhang J, Wang H, Lyulko OV, Xu Y, Schaefer J, Simaan N, Randers-Pehrson G, Yao YL, Garty G. 2011. Adapting the γ -H2AX assay for automated processing in human lymphocytes. 1. Technological aspects. *Radiation Research* 175:282–290.